

Article

Single crystal growth of YbRh_2Si_2 and YbIr_2Si_2

Cornelius Krellner^{a,b,†}, Sebastian Taube^{a,‡}, Tanja Westerkamp^{a,§}, Zakir Hossain^c, and Christoph Geibel^a

^a*Max Planck Institute for Chemical Physics of Solids, D-01187 Dresden, Germany*

^b*Cavendish Laboratory, University of Cambridge, Cambridge CB3 0HE, United Kingdom*

^c*Department of Physics, Indian Institute of Technology, Kanpur 208016, India*
(October 16, 2018)

We report on the single crystal growth of the heavy-fermion compounds YbRh_2Si_2 and YbIr_2Si_2 using a high-temperature indium-flux technique. The optimization of the initial composition and the temperature-time profile lead to large (up to 100 mg) and clean ($\rho_0 \approx 0.5 \mu\Omega\text{cm}$) single crystals of YbRh_2Si_2 . Low-temperature resistivity measurements revealed a sample dependent temperature exponent below 10 K, which for the samples with highest quality deviates from a linear-in- T behaviour. Furthermore, we grew single crystals of the alloy series $\text{Yb}(\text{Rh}_{1-x_{\text{Ir}}}\text{Ir}_{x_{\text{Ir}}})_2\text{Si}_2$ with $0 \leq x_{\text{Ir}} \leq 0.23$ and report the structural details. For pure YbIr_2Si_2 , we establish the formation of two crystallographic modifications, where the magnetic $4f$ -electrons have different physical ground states.

Keywords: YbRh_2Si_2 , YbIr_2Si_2 , Metal-flux technique, Kondo-lattice systems, Quantum critical point

1. Introduction

Most of the ternary intermetallic compounds with the chemical formula AT_2X_2 (A = alkaline earth metals, lanthanides or actinides, T = transition metal and X = B, Ga, Si, Ge, Sn, P, As, ...) crystallize in ternary variants of the tetragonal body-centred BaAl_4 structure type, usually in the ThCr_2Si_2 -structure one [1, 2]. Characteristic of this structure are layers of edge-connected TX_4 -tetrahedra, which alternate along the c -direction with planar square lattices of A -atoms. Prominent examples, concerning their physical properties, are CeCu_2Si_2 [3], URu_2Si_2 [4] and SrFe_2As_2 [5], which all are model systems among the field of strongly correlated electron systems.

Within this field, the discovery of remarkable phases and transitions is often tightly coupled to the growth and characterization of novel materials. Studying these emergent phenomena necessitate the preparation of high-quality single crystals to investigate the physical properties as a function of crystal orientation and momentum. Here, we report on the details of the single crystal growth of pure YbRh_2Si_2 and YbIr_2Si_2 as well as the alloy series $\text{Yb}(\text{Rh}_{1-x_{\text{Ir}}}\text{Ir}_{x_{\text{Ir}}})_2\text{Si}_2$, using a high-temperature indium-flux technique. The growth of sizeable single crystals of these compounds is challenging, because of the high vapour pressure of Yb, whose boiling point, 1196°C , is well below the melting point of Rh (1964°C) or Ir (2466°C).

[†]Corresponding author. Email: krellner@cpfs.mpg.de

[‡]Present address: Siltronic AG, D-09599 Chemnitz, Germany

[§]Present address: Deutsches Biomasseforschungszentrum, D-04347 Leipzig, Germany

Thus, the growth from a stoichiometric melt is likely impossible. Furthermore, the solubility of Si, Rh and Ir in the most appropriate low-melting solvents, In and Sn, is small, making the growth of large crystals rather difficult.

YbRh_2Si_2 also crystallizes in the ThCr_2Si_2 structure [6] and was intensively studied in recent years, because it is situated on the magnetic side ($T_N = 72$ mK) of, but very close to a quantum critical point (QCP). The proximity to the QCP leads to pronounced non-Fermi-liquid behavior in transport and thermodynamic properties, such as the divergence of the electronic Sommerfeld coefficient, $\gamma = C^{4f}/T$, and a linear-in- T resistivity [7]. The weak antiferromagnetic (AFM) order can be continuously suppressed by applying a tiny magnetic field [8, 9]. Electrical transport and thermodynamic measurements have revealed multiple vanishing energy scales [10] and, when the finite-temperature results are extrapolated to the $T = 0$ limit, a discontinuity of the Fermi volume across the QCP [11–13].

A specific feature of the YbRh_2Si_2 single crystals are their suitability to cleave, yielding atomically flat and clean surfaces perpendicular to the crystallographic c -direction. This made extensive angle-resolved photo-emission spectroscopy possible, which gives significant insight into the heavy-fermion behaviour of $4f$ -based correlated systems [14–16]. Recent tunneling-spectroscopy experiments succeeded to directly image the transformation into the coherent ground state of the Kondo lattice [17].

The isoelectronic compound YbIr_2Si_2 crystallizes in two different structure types, the ThCr_2Si_2 and the CaBe_2Ge_2 [18]. In the latter, an Ir- and Si-plane are interchanged with each other, therefore, the CaBe_2Ge_2 structure has a lower symmetry, with a missing mirror plane around the body centred Yb-atom. This structure is therefore named primitive (or P-type) in contrast to the body-centred (I-type) version. In Fig.1, both structure types are presented and one clearly can see the interchanged Ir-/Si-atoms in the lower Ir-Si-plane.

Low-temperature resistivity and specific-heat measurements of I-type YbIr_2Si_2 show strong similarities with YbRh_2Si_2 . However below 200 mK, I-type YbIr_2Si_2 presents a magnetically non-ordered Fermi-liquid ground state and is situated on the paramagnetic side of the QCP. A larger unit-cell volume, compared to YbRh_2Si_2 , results in a higher Kondo-energy scale, leading to a Kondo-screened ground state. Therefore, the series $\text{Yb}(\text{Rh}_{1-x_{\text{Ir}}}\text{Ir}_{x_{\text{Ir}}})_2\text{Si}_2$ is well suited to study the physical properties across this QCP. First studies revealed a detaching of the AFM QCP from the Fermi-surface reconstruction and a new spin-liquid-type ground state for $x_{\text{Ir}} = 0.06$ and 0.17 [19, 20]. On the other hand, P-type YbIr_2Si_2 orders antiferromagnetically at $T_N \approx 0.6$ K and do not present any non-Fermi-liquid characteristics [21].

2. Single crystal growth

2.1. Experimental

The single crystal growth of YbRh_2Si_2 and YbIr_2Si_2 was achieved using an In-flux technique [7, 18, 22]. Yb ingots (Ames, 99.99%), Rh/Ir powder (Heraeus, 99.95%), Si pieces (Alfa Aesar, 99.9999%) and In shots (Alfa Aesar, 99.9999%) were put together in a conical Al_2O_3 -crucible ($V \approx 30$ ml). The Yb was stored and weighted in a glove box filled with purified argon gas. Great care was undertaken to keep the oxygen and water content below 0.1 ppm. Afterwards, the Al_2O_3 -crucible was enclosed in a Ta-tube, again under very pure Ar-atmosphere, using arc welding. Subsequently, the Ta-tube was put under Ar in a vertical high-temperature resistance furnace, where temperatures of up to 1600°C could be achieved. The tem-

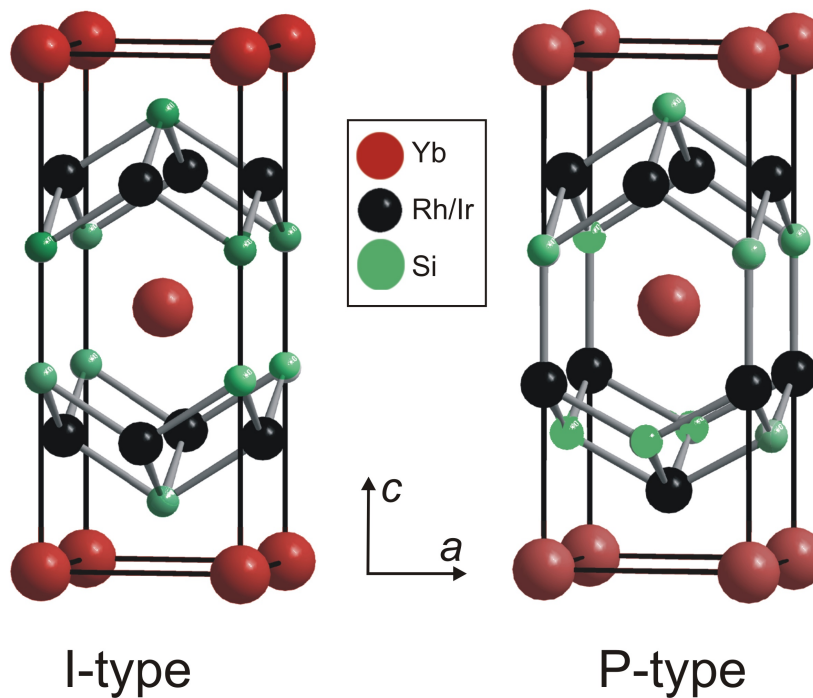


Figure 1. Unit cell of the ThCr_2Si_2 and the CaBe_2Ge_2 structure types, denoted as I-type and P-type, respectively. YbRh_2Si_2 crystallizes with the I-type structure, whereas, both structures form in the case of YbIr_2Si_2 .

perature was measured in-situ at the bottom of the crucible, independently of the furnace temperature. For cooling, a modified Bridgman technique was utilized by slowly moving the Ta-tube out of the furnace with velocities as low as 0.1 mm/h. After the growth, the In-flux was removed by etching the solidified melt in slightly diluted hydrochloric acid at moderate temperatures ($\approx 60^\circ\text{C}$). This dissolves also most of the binary and ternary foreign phases which has been formed due to the off-stoichiometric starting composition. The YbT_2Si_2 single crystals were found to be very stable in HCl, therefore, a complete etching for 1-2 days was possible. Finally, the single crystals were rinsed in an ultrasonic bath using acetone.

2.2. YbRh_2Si_2

The growth of YbRh_2Si_2 single crystals from a tin-flux was already reported in the first publication of its low-temperature properties in 2000 [7]. In the meantime, comprehensive studies were carried out on this model-type quantum-critical material, as discussed in the introduction. Most of these measurements were performed on single crystals, obtained from an improved flux-growth process, however, a description of the growth parameters was not yet reported. In this section, we discuss in detail the parameters of this high-temperature tin-flux technique. Many of the aforementioned experiments were possible only, because of the larger and purer single crystals obtained after the optimization.

Two different research groups have also been working on the single crystal growth of YbRh_2Si_2 . Knebel *et al.* have grown mono-isotopic $^{174}\text{YbRh}_2\text{Si}_2$ single crystals from In-flux with a residual resistivity, $\rho_0 \approx 1.3 \mu\Omega\text{cm}$, as well as very pure non-mono-isotopic crystals [23]. On the latter, de-Haas-van-Alphen and resistivity measurements under pressure were performed. Hu *et al.* reported on very large single crystals, which could be obtained using Zn-flux [24]. However, these crystals present only a residual resistivity, $\rho_0 \approx 8 \mu\Omega\text{cm}$, likely resulting from Zn-incorporation and

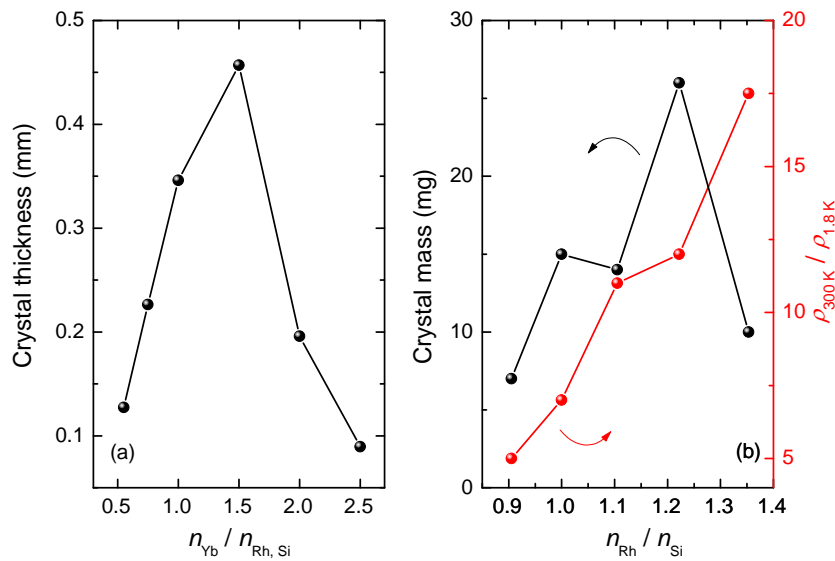


Figure 2. Optimization of the initial stoichiometry of YbRh_2Si_2 . (a) Influence of the Yb-content on the average crystal thickness. (b) Influence of the Rh-to-Si ratio, $n_{\text{Rh}}/n_{\text{Si}}$, on the average crystal mass (left axis) and the resistivity ratio, $\rho_{300\text{K}}/\rho_{1.8\text{K}}$ (right axis).

no further physical measurements were published until now.

The optimization of the single crystal growth from a metallic flux focuses mainly on two parameters. Firstly, the initial stoichiometry and secondly, the temperature-time profile of the crystal growth. These two parameter classes are not independent from each other, therefore, we first have optimized the initial stoichiometry and in a second step determined the best-possible temperature-time profile.

In the first step, we have varied the initial atomic composition of Yb, Rh and Si with respect to each other, but kept the mass ratio to the amount of In-flux constant, with $m_{\text{In}}/m_{\text{Yb,Rh,Si}} = 24M_{\text{In}}/M_{\text{Yb,Rh,Si}}$. Here, $m_{\text{Yb,Rh,Si}}$ is the sum of the mass of Yb, Rh and Si, M_{In} is the molar mass of indium, and $M_{\text{Yb,Rh,Si}}$ is the molar mass of Yb, Rh and Si in the given composition (e.g., for Yb:Rh:Si = 3:2:2, $M_{\text{Yb,Rh,Si}} = 781.1\text{ g/mol}$). During variation of the stoichiometry, we kept all other growth parameters constant.

In Fig. 2a, we present the influence of the Yb-content on the crystal thickness, \bar{d} , where we take an average value for the 10 largest crystals of each batch. The Yb-content could be varied in a broad range from 1:2:2 to 5:2:2 (Yb:Rh:Si). In all cases stoichiometric YbRh_2Si_2 single crystals are formed, however, the different Yb-content of the initial melt leads to single crystals with different thicknesses. From Fig. 2a it is evident that the thickest crystals ($\bar{d} \approx 0.45\text{ mm}$) could be obtained with a three-times higher Yb-content, i.e. ($n_{\text{Yb}}/n_{\text{Rh,Si}} = 1.5$). For higher Yb-contents, the thickness decreases and for $n_{\text{Yb}}/n_{\text{Rh,Si}} = 2.5$ only very tiny single crystals are formed.

In a next step, we have optimized the ratio of Rh to Si, while keeping $n_{\text{Yb}}/n_{\text{Rh,Si}} = 1.5$ constant. Here we learned, that the applicable range is much narrower, compared to the Yb one. The $n_{\text{Rh}}/n_{\text{Si}}$ ratio can only be varied from 0.9 to 1.35. In this range several crystal growths were carried out, with otherwise identical parameters. We found that the mass of the crystals, \bar{m} , (again we take an average over the 10 largest crystals) is largest at $n_{\text{Rh}}/n_{\text{Si}} \approx 1.22$ corresponding to an initial ratio of Yb:Rh:Si = 3:2.2:1.8 (Fig. 2b, left axis). The thickness is nearly constant from $n_{\text{Rh}}/n_{\text{Si}} = 1$ to 1.22 ($\bar{d} \approx 0.5\text{ mm}$) but considerably smaller ($\bar{d} \approx 0.3\text{ mm}$) for $n_{\text{Rh}}/n_{\text{Si}} = 0.9$ and $n_{\text{Rh}}/n_{\text{Si}} = 1.35$. More important is the influ-

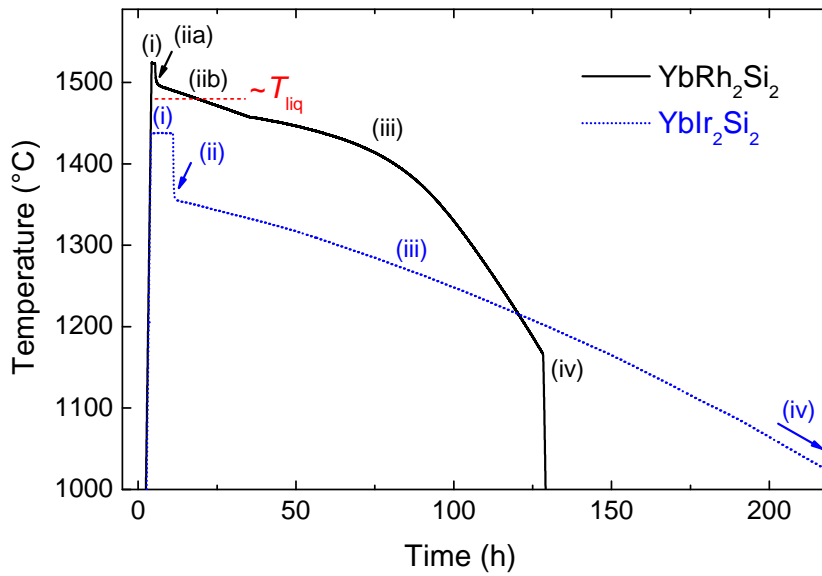


Figure 3. Optimized temperature-time profile for the single crystal growth of YbRh_2Si_2 and YbIr_2Si_2 . The temperature was measured in-situ at the bottom of the crucible.

ence on the crystal quality, reflected in the resistivity ratio at 1.8 K, $\rho_{300\text{K}}/\rho_{1.8\text{K}}$, which increases from 5 for excess Si to 17.5 for $n_{\text{Rh}}/n_{\text{Si}} = 1.35$ (Fig. 2b, right axis). However, YbRh_2Si_2 is not anymore the main phase using this high Rh-content and YbRhIn_5 is formed instead. This is reflected in overall much smaller and thinner crystals for $n_{\text{Rh}}/n_{\text{Si}} = 1.35$. Therefore, we decided to continue the optimization procedure of the temperature profile with the atomic ratio Yb:Rh:Si = 3:2.2:1.8.

Differential-thermal-analysis measurements were carried out to determine the liquidus temperature of YbRh_2Si_2 in 96 mol% In. We found an anomaly in the cooling curve at $T_{\text{liq}} \approx 1480^\circ\text{C}$, which most likely is due to the formation of YbRh_2Si_2 within the liquid indium. From several growths, not following a systematic optimization procedure, we observed that a reduction of the time at highest temperatures results in higher-quality single crystals. Therefore, we have optimized the temperature-time profile, which includes several steps (solid line in Fig. 3), by using a vertical two-zone furnace (Xerion company).

First, we heated both zones to reach a temperature of 1520°C throughout the crucible for one hour (step (i) in Fig. 3). Subsequently, a temperature gradient was build up within the crucible by moving the sample out of the furnace (step (ia)) and by slowly decreasing the power of the lower heating zone (step (iib)). Finally, we start the Bridgman-type cooling by moving the Ta-tube further out of the furnace, whereas the higher heating zone is kept at its initial temperature (step (iii)). The crystal growth is finished at around 1150°C and the furnace is cooled down to room temperature (step (iv)).

We assume that the following processes take place: Step (i) provides an homogenization of the melt at temperatures well above T_{liq} . The first seeds of YbRh_2Si_2 can form at the bottom of the crucible when the temperature goes through T_{liq} (step (iib)). We use the second heating zone to build up a temperature gradient inside the crucible, which significantly reduces the total time at high temperatures. The crystal grow during step (iii), where the temperature-time curve has at the beginning a much smaller slope. In contrast to a normal Bridgman technique without a metallic flux, here, several seeds form at the bottom of the crucible, which result in many crystals of comparable size and quality.

The optimization of the temperature-time profile leads to single crystals with

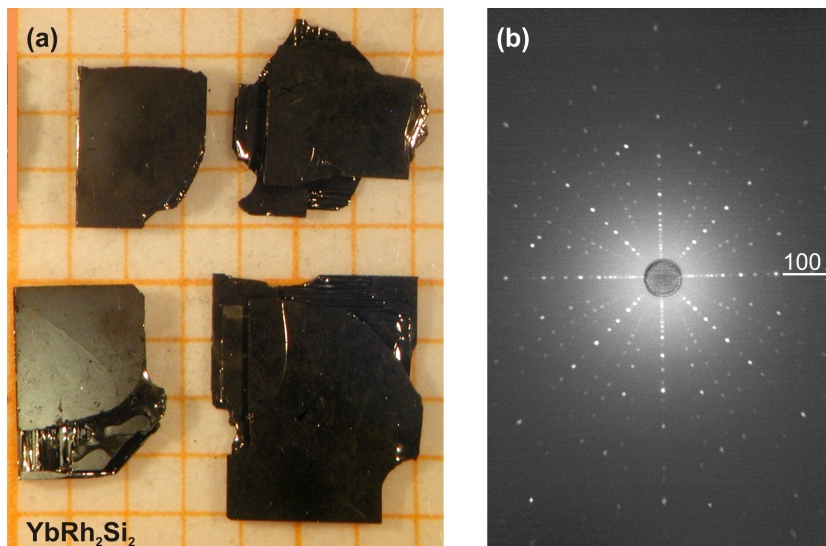


Figure 4. (a) Photograph of high-quality YbRh_2Si_2 single crystals. The edges are statistically aligned along 100 and 110, which can be proved by Laue back scattering images plotted in (b). Here, the horizontal direction corresponds to the 100 direction.

much higher resistivity ratios, reaching $\rho_{300\text{K}}/\rho_{1.8\text{K}} = 27$. Some of these crystals are pictured in Fig. 4a. These new generation of single crystals were deeply investigated at low temperatures and reveal a broad range of exciting physical phenomena. The residual resistivity, extracted from measurements down to the mK range, reaches $\rho_0 \approx 0.5 \mu\Omega\text{cm}$ resulting in a resistivity ratio as high as $\rho_{300\text{K}}/\rho_0 \approx 150$ [25]. The extremely sharp anomaly in the specific heat at T_N is a further proof of the high quality [26]. Directly visible is the low defect density of these crystals in recent scanning tunneling measurements [17], where large areas of defect-free surfaces could be resolved. Some of the few defects could be assigned to Rh occupation on Si-sites, in agreement with the slight Rh excess described above. In contrast, single crystals prepared with excess Si show a lot more defects at the surface [27], which confirms that the resistivity ratio is a valid measure to access the quality of the crystals.

2.3. YbIr_2Si_2

The growth of the related compound YbIr_2Si_2 is possible using a similar high-temperature In-flux method [18]. Here, we used an one-zone resistance furnace and a slightly different temperature-time profile during the crystal growth (see dotted curve in Fig. 3). The homogenization (step (i)) is done for 8 hours at 1450°C . The temperature gradient was build up by moving the sample out of the furnace, which leads to a temperature jump of 100°C ((step (ii) in Fig. 3). Subsequently, we start the Bridgman-type cooling by slowly moving the sample tube further out of the furnace (step (iii)). After 300 hours, the crystal growth is terminated at around 800°C .

Using a stoichiometric composition of the elements with 96 mol% indium, gives quite large crystals with an average mass of 35 mg and an average thickness of 0.6 mm. Furthermore, the purest crystals obtained without optimization have already a residual resistivity of only $\rho_0 \approx 0.3 \mu\Omega\text{cm}$ giving a resistivity ratio, $\rho_{300\text{K}}/\rho_0 \approx 225$ [18].

The reproducibility of the growth process is not as good as for YbRh_2Si_2 . Nearly identical growth parameters lead sometimes to large but also to small crystals, mak-

Table 1. Parameters and results of the crystal growth of $\text{Yb}(\text{Rh}_{1-x_{\text{Ir}}}\text{Ir}_{x_{\text{Ir}}})_2\text{Si}_2$.

Initial composition Yb : Rh : Ir : Si	$x_{\text{Ir}}^{\text{nom}}$	$x_{\text{Ir}}^{\text{EDAX}}$	\bar{d} (mm)	\bar{m} (mg)	$\frac{\rho_{300\text{K}}}{\rho_{1.8\text{K}}}$
3 : 1.96 : 0.04 : 2.0	0.02	0.025	0.4	13	7.1
3 : 1.90 : 0.10 : 2.0	0.05	0.06	0.2	4	6.5
3 : 1.60 : 0.40 : 2.0	0.2	0.17	0.3	4	3.9
3 : 1.68 : 0.42 : 1.9	0.2	0.23	0.2	6	4.1

ing a quantitative optimization very difficult. However, we varied also for YbIr_2Si_2 the initial composition and found that the applicable ranges are much smaller than for YbRh_2Si_2 . Doubling the Yb-content, $n_{\text{Yb}}/n_{\text{Ir,Si}} = 1$, do not yield YbIr_2Si_2 crystals anymore, instead binary phases as e.g., YbIn_2 , YbIr_3 and Yb_5Si_3 are formed. A small excess of Yb, $n_{\text{Yb}}/n_{\text{Ir,Si}} = 0.6$, leads to the formation of P-type YbIr_2Si_2 . Using an off-stoichiometric ratio of Ir to Si, $n_{\text{Ir}}/n_{\text{Si}} = 1.22$, do no result in YbIr_2Si_2 crystals but to the formation of some unknown phases. From these results it is obvious that the optimal crystal growth parameters are much different in YbRh_2Si_2 and YbIr_2Si_2 . However, the present output, concerning size and quality of the YbIr_2Si_2 crystals is already satisfactory, so no further optimization was undertaken.

The formation of the two structural variants, I-type and P-type, in YbIr_2Si_2 is not surprising, because these two different structures were observed in other RIr_2Si_2 compounds as well [28–31]. There, it was established, that the P-type configuration forms only at high temperatures, whereas the I-type is stabilized at lower temperatures. Here, we are mainly interested in the I-type structure which is isostructural to YbRh_2Si_2 . Therefore, we have chosen the temperature-time profile such that a long annealing time below 1000°C was achieved (see Fig. 3). It is presently unclear, why the excess of Yb leads to the stabilization of the P-type phase. However, we were able to transform the P-type single crystals into I-type by annealing the crystals at 1000°C for 150 hours. For this purpose the crystals extracted from the In-flux were enclosed in a Ta-crucible under argon at ambient pressure. We discuss the differences of I- and P-type in the X-ray diffraction patterns and the different physical ground states in the sections 3.2 and 4.2, respectively.

2.4. $\text{Yb}(\text{Rh}_{1-x_{\text{Ir}}}\text{Ir}_{x_{\text{Ir}}})_2\text{Si}_2$

As stated above, negative chemical pressure has to be applied to YbRh_2Si_2 to reach the QCP in the absence of external magnetic field. This can be achieved by various kind of substitutions. Ge-substitution on the Si site was tried first [9, 32], however, the maximal substitution level amounts to only about 2 at% [33]. Higher substitution can be achieved replacing the magnetic Yb-atoms with non-magnetic La [34] or Lu [35]. Here, we discuss a further substitution series, $\text{Yb}(\text{Rh}_{1-x_{\text{Ir}}}\text{Ir}_{x_{\text{Ir}}})_2\text{Si}_2$, where the Rh atoms are replaced by the larger isoelectronic Ir-atoms.

For the crystal growth of $\text{Yb}(\text{Rh}_{1-x_{\text{Ir}}}\text{Ir}_{x_{\text{Ir}}})_2\text{Si}_2$ we used the optimized growth parameters of YbRh_2Si_2 , with the respective replacement of Rh by Ir. The initial stoichiometry together with the properties of the resulting single crystals are given in Table 1. For all growths the amount of In-flux was kept constant as described above, with $m_{\text{In}}/m_{\text{Yb,Rh,Ir,Si}} = 24M_{\text{In}}/M_{\text{Yb,Rh,Ir,Si}}$.

The Ir content was determined using energy dispersive X-ray (EDAX) spectra obtained in a scanning electron microscope (Philips XL30) with a Si(Li)-X-ray detector. Three crystals of each batch with a polished surface were analyzed at several positions. The respective mean values result in the given $x_{\text{Ir}}^{\text{EDAX}}$ values with an absolute error of less than 0.01. These real Ir-concentrations, which are used for x_{Ir} throughout this article, are somewhat different than the nominal concentrations,

$x_{\text{Ir}}^{\text{nom}}$, due to different solubilities of the elements in the In-flux. The average thickness and mass of the single crystals are again determined by averaging over the 10 largest crystals. The resistivity ratio, $\rho_{300\text{K}}/\rho_{1.8\text{K}}$, reflects the amount of disorder in the single crystals.

Unfortunately, the size of the crystals gets smaller with increasing Ir-content, opposite to what was observed for the $\text{Yb}(\text{Rh}_{1-x_{\text{Co}}}\text{Co}_{x_{\text{Co}}})_2\text{Si}_2$ series, where the crystal growth gives larger crystals, with increasing x_{Co} [36]. The value of the resistivity ratio decreases with increasing x_{Ir} , which is expected due to the higher amount of disorder introduced by the statistical occupation of the Ir atoms at the Rh site. An exception is the growth with $x_{\text{Ir}} = 0.23$, because $\rho_{300\text{K}}/\rho_{1.8\text{K}}$ is somewhat larger than for $x_{\text{Ir}} = 0.17$. This is most probably caused by the higher Rh/Ir-content with respect to Si ($n_{\text{Rh+Ir}}/n_{\text{Si}} = 1.1$), similar to what was observed in the pure YbRh_2Si_2 , where we found a larger resistivity ratio for higher Rh-content (see Fig. 2).

3. X-ray diffraction

3.1. YbRh_2Si_2

A series of 10 samples of different quality has been systematically analyzed by X-ray diffraction and electron microprobe analysis. The lattice parameters were accurately determined in respect to the chemical composition and the homogeneity range of the phase YbRh_2Si_2 was defined. These results and the experimental details will be published elsewhere [27].

In Fig. 4b, we present a X-ray Laue backscattering image from a YbRh_2Si_2 single crystal. The reflection peaks are pin sharp rather than blurred, proving again the high quality of the synthesized crystal. These pictures were used to orient the single crystals. In all cases, the direction perpendicular to the surface corresponds to the crystallographic c -axis, proved by the fact that the 001 reflection is exactly in the middle of the aperture. Simulations demonstrate that the horizontal direction corresponds to the 100 direction, which however, not always corresponds to the edges of the crystal, visible in Fig. 4a. Our experience from the orientation of more than 100 of these crystals for photo-emission spectroscopy, revealed that the crystal edges much more often corresponds to the 110 direction, although not exclusively.

3.2. YbIr_2Si_2

The distinction between the body-centred and the primitive structure type of YbIr_2Si_2 is possible using powder X-ray diffraction, which was performed on a Stoe diffractometer in transmission mode using monochromated Cu-K_α radiation ($\lambda = 1.5406 \text{ \AA}$). For the primitive structure additional peaks ($hkl = 001, 003, 102, 111$) are observable. For the body-centred structure these peaks with an odd sum of hkl are absent.

In Fig. 5 we present three different diffractograms for a) pure I-type YbIr_2Si_2 , b) I-type with small content of P-type and c) mainly P-type. The diffraction pattern of the annealed single crystals only show very tiny odd hkl peaks, confirming that in this case we have virtually pure I-type crystals. When the crystal growth is terminated before YbIr_2Si_2 is completely transformed into the I-type structure, the diffraction pattern presents small peaks at the $hkl = 001, 003, 102, 111$ positions (arrows in Fig. 5b). The growth with Yb-excess leads to P-type YbIr_2Si_2 , the corresponding pattern is shown in Fig. 5c. Here, the intensities of the peaks have changed considerably and all odd hkl peaks are observed. However with powder

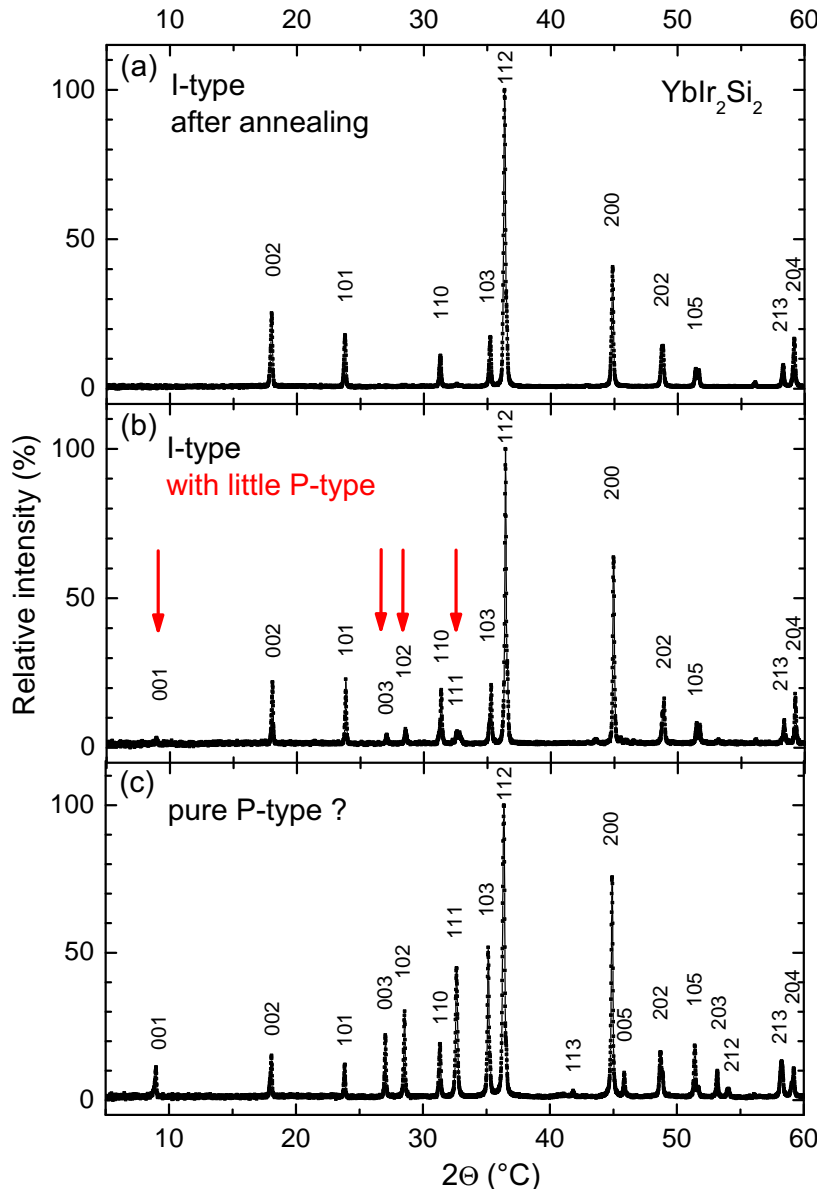


Figure 5. Comparison of three different X-ray powder diffraction patterns of YbIr_2Si_2 . (a) I-type after annealing. (b) I-type with small amount of P-type, leading to additional peaks at $hkl = 001, 003, 102, 111$ (arrows). (c) P-type pattern; the intensities of the peaks have changed considerably and all odd hkl are observed. However, small amount of I-type within the P-type phase cannot be excluded.

diffraction, we cannot finally prove, whether parts of the P-type crystal are already transformed into I-type. This is because the lattice parameters of the two structures are nearly identical with $a_I = 4.0345(15) \text{ \AA}$, $a_P = 4.0370(20) \text{ \AA}$ and $c_I = 9.828(2) \text{ \AA}$, $c_P = 9.898(5) \text{ \AA}$, which were refined by simple least squares fitting.

3.3. $\text{Yb}(\text{Rh}_{1-x_{\text{Ir}}}\text{Ir}_{x_{\text{Ir}}})_2\text{Si}_2$

In Fig. 6 the lattice parameters a (left axis) and c (right axis) are plotted for the different Ir-concentrations. An important point is immediately visible, namely that a and c have opposite trends with increasing x_{Ir} . The lattice parameter a , which describes the distance of the Yb-ions in the plane (see Fig. 1), increases linearly with x_{Ir} and can be described with $a_{\text{Fit}}(\text{ \AA}) = 4.011 + 0.023 \cdot x_{\text{Ir}}$. In contrast, c decreases linearly, with $c_{\text{Fit}}(\text{ \AA}) = 9.860 - 0.034 \cdot x_{\text{Ir}}$. The resulting volume of the

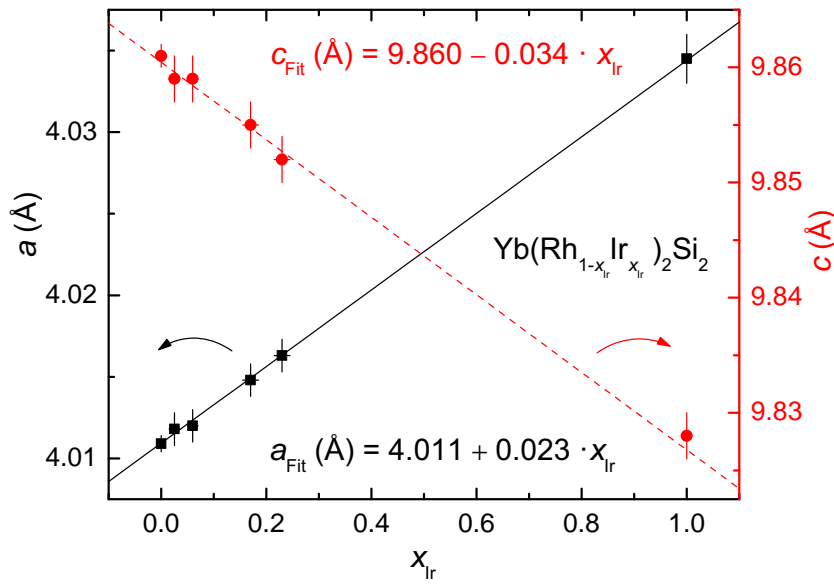


Figure 6. Lattice parameters a (left axis) and c (right axis) for the $\text{Yb}(\text{Rh}_{1-x_{\text{Ir}}}\text{Ir}_{x_{\text{Ir}}})_2\text{Si}_2$ series. With increasing Ir content, a linearly increases, whereas c decreases.

unit cell increases with increasing x_{Ir} , however, the overall volume change going from YbRh_2Si_2 to YbIr_2Si_2 amounts to only $\Delta V = 1.3(2) \text{ \AA}^3$, which is less than 1%. This is a rather small increase of the unit cell volume, because the variation of a and c cancels out each other. The corresponding hydrostatic pressure, if applied to YbIr_2Si_2 , amounts to $p \approx 1.6 \text{ GPa}$, using a bulk modulus of 190 GPa [37]. However, for increasing Ir-concentration, the ratio of the lattice parameters, c/a , strongly decreases, as c decreases and a increases with x_{Ir} . This results in a distortion of the unit cell, which gets less elongated with higher Ir-content. Therefore, isoelectronic substitution is not equivalent to hydrostatic pressure, which would result in a constant c/a ratio. This is probably the reason why for YbIr_2Si_2 a huge pressure of 8 GPa is needed to induce magnetic order [38], in contrast to the expected 1.6 GPa mentioned above. However, for small x_{Ir} the relative change of c/a is less than 0.1%, compared to pure YbRh_2Si_2 , so that small Ir-substitution is equivalent to hydrostatic pressure [19, 39].

4. Physical characterization

4.1. Temperature exponent of the electrical resistivity in YbRh_2Si_2

One of the hallmarks of non-Fermi-liquid behaviour in YbRh_2Si_2 is the linear-in- T resistivity over more than an order of magnitude in temperature. However, this was studied in a wider temperature range only for the very first generation of single crystals with $\rho_0 \approx 2.4 \mu\Omega\text{cm}$ [7]. Here, we present an analysis of the temperature exponent of the resistivity for one of the optimized single crystals with a residual resistivity as low as $\rho_0 \approx 0.5 \mu\Omega\text{cm}$. In zero magnetic field, the resistivity shows a sharp drop at the AFM phase transition ($T_N = 70 \text{ mK}$) but a small critical magnetic field ($B_c = 50 \text{ mT}$, $B \parallel j \perp c$) can be applied to tune the system towards quantum criticality, where the non-Fermi-liquid behaviour is observed down to lowest temperatures [25].

Generally, the temperature dependence of the resistivity can be described with $\Delta\rho(T) = \rho(T) - \rho_0 \propto T^\varepsilon$. Therefore, the temperature exponent, ε , can be visualized by plotting $\partial \ln \Delta\rho(T) / \partial \ln T$, shown in Fig. 7 for two samples with different

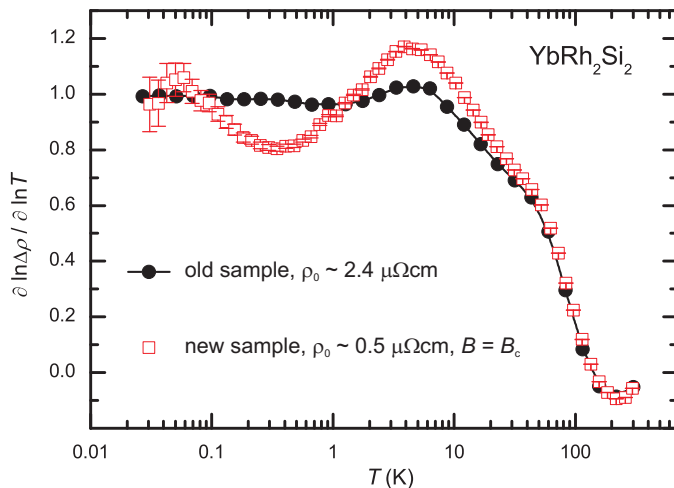


Figure 7. Temperature dependence of the electrical-resistivity exponent, $\varepsilon = \frac{\partial \ln \Delta \rho(T)}{\partial \ln T}$, for two single crystals with different residual resistivity. With higher sample quality (lower ρ_0) pronounced deviations from the linear-in- T resistivity are evident below 10 K.

residual resistivity. The data for the old sample presents a nearly constant $\varepsilon = 1$ below 7 K, down to lowest measured temperatures. In contrast, the exponent of the new sample exhibits a pronounced maximum at around 4 K with $\varepsilon \approx 1.2$, followed by a minimum around 0.3 K with $\varepsilon = 0.8$ and a value of $\varepsilon = 1$ at lowest temperatures. For this analysis we estimate ρ_0 by linear extrapolation to $T = 0$, however, the choice of ρ_0 influences $\varepsilon(T)$ only at lowest temperatures. This is visible by the larger error bars of ε below 0.1 K, which result from the uncertainty of ρ_0 . Beside this temperature-dependent analysis of the exponent, we additionally fit the data with a single ε in a larger temperature range. For the resistivity data below 0.1 K, we obtain an exponent of $\varepsilon = 1.00 \pm 0.01$. A fit below 0.2 K down to lowest temperatures gives $\varepsilon = 0.831 \pm 0.004$, in agreement with the differential analysis.

We note that the evolution of the exponent for these two different samples presents qualitative similarities to quasi-classical calculations for a system in the vicinity of an antiferromagnetic QCP. There, A. Rosch studied the influence of strong anisotropic scattering due to spin fluctuations for different amount of disorder and he observed broad ranges of exponents between 1 and 2 together with oscillatory behaviour [40]. It might be interesting to implement the specifics of YbRh_2Si_2 to such a model to get further insight into the transport phenomena at this local QCP.

4.2. Different ground states in I-type and P-type YbIr_2Si_2

YbIr_2Si_2 crystallizes in two different structure types, a bodycentred (I-type) and a primitive (P-type) variant (see Fig. 1 and Sec. 2.3). Interestingly, the magnetic ground states of these two derivatives of the BaAl_4 structure are very different, although, the tetragonal lattice parameters are nearly identical, as discussed in Sec. 3.2. Hossain *et al.* have shown that I-type YbIr_2Si_2 is a heavy-fermion metal situated on the non-magnetic side of a QCP with Fermi-liquid behaviour below 0.4 K and quite large single-ion anisotropy, reflected in a larger susceptibility perpendicular to the crystallographic c -direction [18]. On the other hand, the suscep-

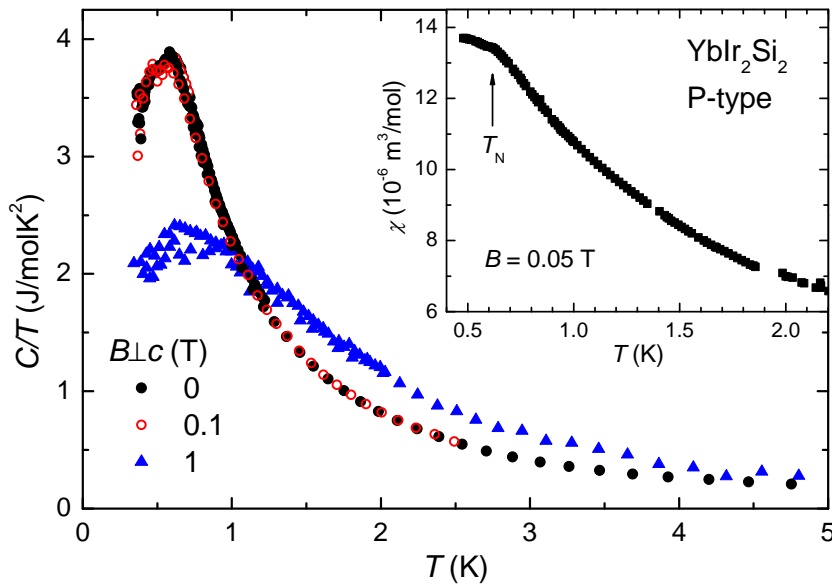


Figure 8. Specific heat divided by temperature, C/T , of YbIr_2Si_2 (P-type) on a linear temperature scale. At $T_N \approx 0.6$ K, a pronounced anomaly is visible which is suppressed in $B = 1$ T. The dc susceptibility, plotted in the inset, confirms the magnetic nature of this phase transition.

tibility of P-type YbIr_2Si_2 is rather isotropic [21] and entropy as well as resistivity measurements suggest a much smaller Kondo-temperature, $T_K^P \approx 2$ K, in contrast to $T_K^I \approx 40$ K for the I-type system [18]. Furthermore, in P-type crystals a prominent anomaly was observed in the specific heat below 1 K, which was suggested to be a magnetic phase transition.

Here, we further like to establish that P-type YbIr_2Si_2 indeed orders antiferromagnetically at $T_N = 0.6$ K by means of susceptibility measurements below 2 K. For this purpose, P-type crystals were prepared with Yb-excess as described in Sec. 2.3 and the dc susceptibility was measured down to $T = 0.5$ K, which was realized with the ^3He -option for the MPMS (Quantum Design) designed by the IQANTUM Corporation. In the inset of Fig. 8, we present this measurement with $B = 0.05$ T perpendicular to c . A weak anomaly suggests that P-type YbIr_2Si_2 undergoes a magnetic phase transition at $T_N \approx 0.6$ K, although the transition is not very sharp. Specific heat measurements on these crystals confirm the earlier measurements in zero field [18] and are shown in the main part of Fig. 8. Applying a magnetic field of 0.1 T does not affect the anomaly at T_N , whereas a field of $B = 1$ T suppresses the magnetic transition and shifts the entropy to higher temperatures. The characteristics of this field dependence confirms the AFM nature of the phase transition and classifies P-type YbIr_2Si_2 as a magnetically ordered system with localized Yb^{3+} moments. However, the anomalies at T_N are rather broad and we were not able to detect the magnetic transition in low-temperature resistivity measurements, probably due to significant amount of disorder, likely Ir-Si site exchanges.

5. Conclusion

In conclusion, we have optimized the single crystal growth of YbRh_2Si_2 , using an indium-flux method with 96 mol% indium in closed Ta-crucibles. The optimal initial composition of the elements within the flux, $\text{Yb}:\text{Rh}:\text{Si} = 3:2.2:1.8$, is far away from the stoichiometric ratio but was found to give large (up to 100 mg) single crystals. Prior to the optimization of the temperature-time profile, we determined

the liquidus temperature ($T_{\text{liq}} \approx 1480^\circ\text{C}$) of YbRh_2Si_2 in 96 mol% In-flux by means of differential thermal analysis and use a two-zone resistance furnace to reduce the time of the crystal growth. The resulting single crystals have a residual resistivity of only $\rho_0 \approx 0.5 \mu\Omega\text{cm}$ and present sharp anomalies in the transport and thermodynamic properties at the low-lying AFM phase transition. The analysis of the temperature-dependence of the electrical-resistivity exponent for this new generation of single crystals reveals a deviation from the linear-in- T behaviour below 10 K.

YbIr_2Si_2 was established to be a polymorphic compound which can crystallize in two different crystallographic modifications, with P-type crystals (CaBe_2Ge_2 structure) being the high-temperature and I-type (ThCr_2Si_2 structure) the low-temperature phase. The latter can be stabilized by annealing selected crystals at 1000°C for 150 hours. We further found that the optimal growth parameters for YbRh_2Si_2 and YbIr_2Si_2 from In-flux are much different. For YbIr_2Si_2 , the applicable range of the initial composition is very narrow and small excess of Yb leads to the formation of P-type crystals. Interestingly, both modifications have different physical ground states. In P-type YbIr_2Si_2 , the magnetic $4f$ -electrons undergo an AFM phase transition at $T_N \approx 0.6$ K, observed in low-temperature specific-heat and susceptibility measurements, whereas I-type YbIr_2Si_2 presents a paramagnetic Fermi-liquid ground state and is situated on the non-magnetic side of the quantum critical point. The series $\text{Yb}(\text{Rh}_{1-x_{\text{Ir}}}\text{Ir}_{x_{\text{Ir}}})_2\text{Si}_2$, which crystallizes in the I-type structure, is therefore ideally suited to study the phenomena around this quantum phase transition.

Acknowledgements

The authors thank U. Burkhardt and P. Scheppan for energy dispersive X-ray analysis of the samples as well as N. Caroca-Canales and R. Weise for technical assistance. The presented low-temperature susceptibility measurements were performed with the help of C. Klausnitzer. We acknowledge valuable discussions with M. Brando, M. Deppe, J. Ferstl, S. Friedemann, P. Gegenwart, A. Rosch, and F. Steglich. The DFG (Research Unit 960, "Quantum phase transitions") is acknowledged for financial support.

References

- [1] Z. Ban and M. Sikirica, *Acta Cryst.* 18 (1965) p.594.
- [2] R. Hoffmann and C. Zheng, *J. Phys. Chem.* 89 (1985) p.4175.
- [3] O.I. Bodak, G.E. I and K.P. I, *Inorg. Mater.* 2 (1966) p.1861.
- [4] K. Hiebl, C. Horvath, P. Rogl and M. Sienko, *J Magn. Magn. Mater.* 37 (1983) p.287.
- [5] M. Pfisterer and G. Nagorsen, *Z. Naturforsch. B: Chem. Sci.* 35 (1980) p.703.
- [6] D. Rossi, R. Marazza and R. Ferro, *J. Less Comm. Met.* 66 (1979) p.P17.
- [7] O. Trovarelli, C. Geibel, S. Mederle, C. Langhammer, F. Grosche, P. Gegenwart, M. Lang, G. Sparn and F. Steglich, *Phys. Rev. Lett.* 85 (2000) p.626c.
- [8] P. Gegenwart, J. Custers, C. Geibel, K. Neumaier, T. Tayama, K. Tenya, O. Trovarelli and F. Steglich, *Phys. Rev. Lett.* 89 (2002) p.056402.
- [9] J. Custers, P. Gegenwart, H. Wilhelm, K. Neumaier, Y. Tokiwa, O. Trovarelli, C. Geibel, F. Steglich, C. Pepin and P. Coleman, *Nature* 424 (2003) p.524.
- [10] P. Gegenwart, J. Custers, Y. Tokiwa, C. Geibel and F. Steglich, *Phys. Rev. Lett.* 94 (2005) p.076402.
- [11] S. Paschen, T. Lühmann, S. Wirth, P. Gegenwart, O. Trovarelli, C. Geibel, F. Steglich, P. Coleman and Q. Si, *Nature* 432 (2004) p.881.
- [12] S. Friedemann, N. Oeschler, S. Wirth, C. Krellner, C. Geibel, F. Steglich, S. Paschen, S. Kirchner and Q. Si, *Proc. Natl. Acad. Sci. USA* 107 (2010) p.14547.
- [13] S. Hartmann, N. Oeschler, C. Krellner, C. Geibel, S. Paschen and F. Steglich, *Phys. Rev. Lett.* 104 (2010) p.096401.
- [14] S. Danzenbächer, Y. Kucherenko, D.V. Vyalikh, M. Holder, C. Laubschat, A.N. Yaresko, C. Krellner, Z. Hossain, C. Geibel, X.J. Zhou, W.L. Yang, N. Mannella, Z. Hussain, Z.X. Shen, M. Shi, L. Patthey and S.L. Molodtsov, *Phys. Rev. B* 75 (2007) p.045109.

- [15] D.V. Vyalikh, S. Danzenbächer, A.N. Yaresko, M. Holder, Y. Kucherenko, C. Laubschat, C. Krellner, Z. Hossain, C. Geibel, M. Shi, L. Patthey and S.L. Molodtsov, *Phys. Rev. Lett.* 100 (2008) p.056402.
- [16] D.V. Vyalikh, S. Danzenbächer, Y. Kucherenko, K. Kummer, C. Krellner, C. Geibel, M.G. Holder, T.K. Kim, C. Laubschat, M. Shi, L. Patthey, R. Follath and S.L. Molodtsov, *Phys. Rev. Lett.* 105 (2010) p.237601.
- [17] S. Ernst, S. Kirchner, C. Krellner, C. Geibel, G. Zwirnagl, F. Steglich and S. Wirth, *Nature* 474 (2011) p.362.
- [18] Z. Hossain, C. Geibel, F. Weickert, T. Radu, Y. Tokiwa, H. Jeevan, P. Gegenwart and F. Steglich, *Phys. Rev. B* 72 (2005) p.094411.
- [19] S. Friedemann, T. Westerkamp, M. Brando, N. Oeschler, S. Wirth, P. Gegenwart, C. Krellner, C. Geibel and F. Steglich, *Nature Physics* 5 (2009) p.465.
- [20] S. Friedemann, T. Westerkamp, M. Brando, N. Oeschler, P. Gegenwart, C. Krellner, C. Geibel, S. MaQuilon, Z. Fisk, F. Steglich and S. Wirth, *J. Low Temp. Phys.* 161 (2010) p.67.
- [21] Z. Hossain, C. Geibel, T. Radu, Y. Tokiwa, F. Weickert, C. Krellner, H. Jeevan, P. Gegenwart and F. Steglich, *Physica B* 378-80 (2006) p.74.
- [22] P. Canfield and I. Fisher, *J. Cryst. Growth* 225 (2001) p.155.
- [23] G. Knebel, R. Boursier, E. Hassinger, G. Lapertot, P. Niklowitz, A. Pourret, B. Salce, J. Sanchez, I. Sheikin, P. Bonville, H. Harima and J. Flouquet, *J. Phys. Soc. Jpn.* 75 (2006) p.114709.
- [24] R. Hu, J. Hudis, C. Stock, C.L. Broholm and C. Petrovic, *J. Cryst. Growth* 304 (2007) p.114.
- [25] P. Gegenwart, T. Westerkamp, C. Krellner, M. Brando, Y. Tokiwa, C. Geibel and F. Steglich, *Physica B* 403 (2008) p.1184.
- [26] C. Krellner, S. Hartmann, A. Pikul, N. Oeschler, J.G. Donath, C. Geibel, F. Steglich and J. Wosnitzer, *Phys. Rev. Lett.* 102 (2009) p.196402.
- [27] S. Wirth, S. Ernst, R. Cardoso-Gil, H. Borrmann, S. Seiro, C. Krellner, C. Geibel, S. Kirchner, U. Burkhardt, Yu. Grin, and F. Steglich, *J. Phys.: Cond. Matter* (2011) to be published.
- [28] H.F. Braun, N. Engel and E. Parthé, *Phys. Rev. B* 28 (1983) p.1389.
- [29] B. Buffat, B. Chevalier, M. Tuilier, B. Lloret and J. Etourneau, *Solid State Commun.* 59 (1986) p.17.
- [30] D. Niepmann and R. Pöttgen, *Intermetallics* 9 (2001) p.313.
- [31] M. Mihalik, J. Pospisil, A. Rudajevova, X. Marti, D. Wallacher, A. Hoser, T. Hofmann, M. Divis and V. Sechovsky, *Intermetallics* 19 (2011) p.1622.
- [32] O. Trovarelli, J. Custers, P. Gegenwart, C. Geibel, P. Hinze, S. Mederle, G. Sparn and F. Steglich, *Physica B* 312 (2002) p.401.
- [33] J. Ferstl TU Dresden, Dissertation.
- [34] J. Ferstl, C. Geibel, F. Weickert, P. Gegenwart, T. Radu, T. Lühmann and F. Steglich, *Physica B* 359-361 (2005) p.26.
- [35] U. Köhler, N. Oeschler, F. Steglich, S. Maquilon and Z. Fisk, *Phys. Rev. B* 77 (2008) p.104412.
- [36] C. Klingner, C. Krellner, M. Brando, C. Geibel, F. Steglich, D.V. Vyalikh, K. Kummer, S. Danzenbächer, S.L. Molodtsov, C. Laubschat, T. Kinoshita, Y. Kato and T. Muro, *Phys. Rev. B* 83 (2011) p.144405.
- [37] J. Plessel, M. Abd-Elmeguid, J. Sanchez, G. Knebel, C. Geibel, O. Trovarelli and F. Steglich, *Phys. Rev. B* 67 (2003) p.180403.
- [38] H.Q. Yuan, M. Nicklas, Z. Hossain, C. Geibel and F. Steglich, *Phys. Rev. B* 74 (2006) p.212403.
- [39] M.E. Macovei, M. Nicklas, C. Krellner, C. Geibel and F. Steglich, *J. Phys. Cond. Mat.* 20 (2008).
- [40] A. Rosch, *Phys. Rev. Lett.* 82 (1999) p.4280.